

Effect of rGO Coating on Interconnected Co_3O_4 Nanosheets and Improved Supercapacitive Behavior of $\text{Co}_3\text{O}_4/\text{rGO}/\text{NF}$ Architecture

Tinghui Yao¹ · Xin Guo¹ · Shengchun Qin¹ · Fangyuan Xia¹ · Qun Li¹ · Yali Li¹ · Qiang Chen² · Junshuai Li¹ · Deyan He¹

Received: 13 December 2016 / Accepted: 26 January 2017 / Published online: 17 March 2017
© The Author(s) 2017. This article is published with open access at Springerlink.com

Highlights

- Interconnected Co_3O_4 nanosheets anchored on rGO-coated nickel foam (NF) are facilely synthesized using a green, simple, and low-cost approach.
- Because of the high specific surface area and optimal mesopore size distribution, high specific capacitances of ~ 1016.4 and 767.1 F g^{-1} are achieved for $\text{Co}_3\text{O}_4/\text{rGO}/\text{NF}$ at current densities of 1 and 5 A g^{-1} , respectively.
- Excellent stability with $\sim 95.5\%$ capacity retention at a high current density of 7 A g^{-1} is achieved even after 3000 cycles.

Abstract In this study, the effect of reduced graphene oxide (rGO) on interconnected Co_3O_4 nanosheets and the improved supercapacitive behaviors is reported. By optimizing the experimental parameters, we achieved a specific capacitance of $\sim 1016.4 \text{ F g}^{-1}$ for the $\text{Co}_3\text{O}_4/\text{rGO}/\text{NF}$ (nickel foam) system at a current density of 1 A g^{-1} . However, the $\text{Co}_3\text{O}_4/\text{NF}$ structure without rGO only delivers a specific capacitance of $\sim 520.0 \text{ F g}^{-1}$ at the same current density. The stability test demonstrates that $\text{Co}_3\text{O}_4/\text{rGO}/\text{NF}$ retains $\sim 95.5\%$ of the initial capacitance value even after 3000 charge–discharge cycles at a high current density of

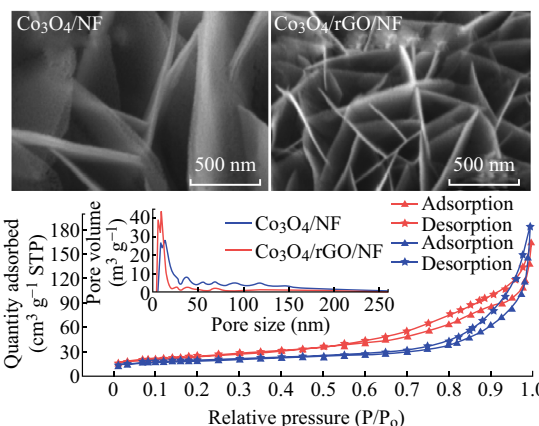
7 A g^{-1} . Further investigation reveals that capacitance improvement for the $\text{Co}_3\text{O}_4/\text{rGO}/\text{NF}$ structure is mainly because of a higher specific surface area ($\sim 87.8 \text{ m}^2 \text{ g}^{-1}$) and a more optimal mesoporous size ($4\text{--}15 \text{ nm}$) compared to the corresponding values of $67.1 \text{ m}^2 \text{ g}^{-1}$ and $6\text{--}25 \text{ nm}$, respectively, for the $\text{Co}_3\text{O}_4/\text{NF}$ structure. rGO and the thinner Co_3O_4 nanosheets benefit from the strain relaxation during the charge and discharge processes, improving the cycling stability of $\text{Co}_3\text{O}_4/\text{rGO}/\text{NF}$.

✉ Junshuai Li
jshli@lzu.edu.cn

✉ Deyan He
hedy@lzu.edu.cn

¹ Key Laboratory of Special Function Materials and Structure Design of the Ministry of Education, Key Laboratory for Magnetism and Magnetic Materials of the Ministry of Education, and School of Physical Science and Technology, Lanzhou University, 222 South Tianshui Road, Lanzhou 730000, People's Republic of China

² Institute of Electromagnetics and Acoustics, Department of Electronic Science, and Fujian Provincial Key Laboratory of Plasma and Magnetic Resonance, Xiamen University, Xiamen 361005, People's Republic of China



Keywords Supercapacitors · rGO · Co_3O_4 nanosheets · Strain relaxation

1 Introduction

In recent years, extensive efforts have been dedicated to research related to supercapacitors owing to their higher power densities, longer cycling performance than Li-ion batteries, and larger energy densities than conventional dielectric capacitors [1–3]. Supercapacitors have a huge potential in applications requiring high-density power and long cycling lifetime such as electric vehicles and portable electronics [4].

Co_3O_4 , an important supercapacitor material, has the advantages of high theoretical capacitance ($\sim 3560 \text{ F g}^{-1}$) [5], low cost, environmental friendliness, and high chemical stability in alkaline electrolytes. It has, thus, attracted much attention recently. Geng et al. [6] prepared porous Co_3O_4 nanoplates with a specific capacitance of $\sim 231 \text{ F g}^{-1}$ at a current density of 1 A g^{-1} using a facile reflux method. Naveen et al. [7] synthesized Co_3O_4 -graphene nanosheets by a chemical method and a high specific capacitance of $\sim 650 \text{ F g}^{-1}$ at a scan rate of 5 mV s^{-1} . However, there still remain some challenges in the practical applications of Co_3O_4 as a high capacity electrode such as poor conductivity and cycling stability, and relatively lower experimental specific capacitances than the theoretical value.

As one kind of nanostructured carbon material, reduced graphene oxide (rGO) has been extensively investigated because of its superior mechanical and electronic properties, high specific surface area, and reasonable chemical stability [8]. These properties make graphene a preferred material for use in supercapacitors and Li-ion batteries as electrode materials and/or active material supporters [9–16]. Therefore, supercapacitors combining nanostructured Co_3O_4 and rGO can be expected to deliver high power and energy densities and long cycling lifetime [15, 17].

In this study, interconnected Co_3O_4 nanosheets anchored onto rGO-coated nickel foam (NF) are facilely synthesized using a green, simple, and low-cost approach. The effect of rGO on the microstructure and improved supercapacitive behaviors of Co_3O_4 nanosheets are investigated here. Because of the large specific area of $\sim 87.8 \text{ m}^2 \text{ g}^{-1}$ and a more optimal mesopore size distribution of $\sim 4\text{--}15 \text{ nm}$, the $\text{Co}_3\text{O}_4/\text{rGO}/\text{NF}$ architecture delivers higher specific capacitances of ~ 1016.4 and 767.1 F g^{-1} at current densities of 1 and 5 A g^{-1} , respectively. In comparison, the $\text{Co}_3\text{O}_4/\text{NF}$ structure has a relatively smaller specific area of $\sim 67.1 \text{ m}^2 \text{ g}^{-1}$ and a less optimal mesopore size distribution of $\sim 6\text{--}25 \text{ nm}$, resulting in lower specific capacitances of ~ 520.0 and 485.8 F g^{-1} at current densities of 1 and 5 A g^{-1} , respectively. Moreover, $\text{Co}_3\text{O}_4/\text{rGO}/\text{NF}$ has excellent

stability, with $\sim 95.5\%$ capacity retention at a high current density of 7 A g^{-1} even after 3000 cycles. This can be attributed to the thinned Co_3O_4 nanosheets and the presence of rGO, improving the electrical and mechanical properties of the $\text{Co}_3\text{O}_4/\text{rGO}/\text{NF}$ system. For $\text{Co}_3\text{O}_4/\text{NF}$, the capacity retention after 3000 cycles at the corresponding current density is about 84.4%.

2 Experimental

2.1 Preparation of the $\text{Co}_3\text{O}_4/\text{rGO}/\text{NF}$ Architecture

Figure 1 shows a schematic illustration of the preparation procedure of the $\text{Co}_3\text{O}_4/\text{rGO}/\text{NF}$ architecture. First, the hydrothermal reduction process is used to prepare rGO-coated NF. After sequential ultrasonic cleaning in acetone, ethanol, and deionized (DI) water each for 10 min, the NFs are dried in air. GO aqueous solution (1.0 mg mL^{-1}) is prepared by dispersing GO, which is prepared by the modified Hummers method [18], into DI water under ultrasonication for 30 min. Then, the GO aqueous solution (10 mL , 1.0 mg mL^{-1}), ascorbic acid (L-AA, 0.02 g), and cleaned NFs of size $2 \times 3 \text{ cm}^2$ are placed into a beaker, which is then heated up to $95 \text{ }^\circ\text{C}$ and kept for 5.0 h for GO reduction and rGO coating onto the NFs. After the beaker is cooled down to room temperature, the products are taken out and dried at $50 \text{ }^\circ\text{C}$ for 3 h [19].

Then, $\text{Co}(\text{OH})_2$ nanosheets are electrochemically deposited at $70 \text{ }^\circ\text{C}$ in a three-electrode cell using rGO-coated NF as the working electrode, a platinum mesh (surface area: $2 \times 2 \text{ cm}^2$) as the counter electrode, and Ag/AgCl (sat. KCl) as the reference electrode. The aqueous electrolyte consists of $0.02 \text{ M Co}(\text{NO}_3)_2 \cdot 6\text{H}_2\text{O}$ and $0.2 \text{ M NH}_4\text{Cl}$. The electrodeposition potential is set at -3.0 V . After 500 s of electrodeposition, the resultant green foam is carefully washed using ethanol and DI water several times and finally dried in air. Then, the product is calcined at $250 \text{ }^\circ\text{C}$ for 2 h in a quartz tube to change $\text{Co}(\text{OH})_2$ into interconnected Co_3O_4 nanosheets [20]. A reference structure of interconnected Co_3O_4 nanosheets anchored onto NF is prepared following a similar process but without the rGO coating procedure, to determine the role of rGO.

2.2 Characterization

The resultant products are characterized by scanning electron microscopy (SEM, MIR A3, TESCAN), high-resolution transmission electron microscopy (HRTEM, FEI Tecnai G² F30), micro-Raman spectroscopy (Jobin-Yvon Horiba HR800 with an excitation wavelength of 532 nm), X-ray powder diffraction (XRD, X'Pert Philips), and

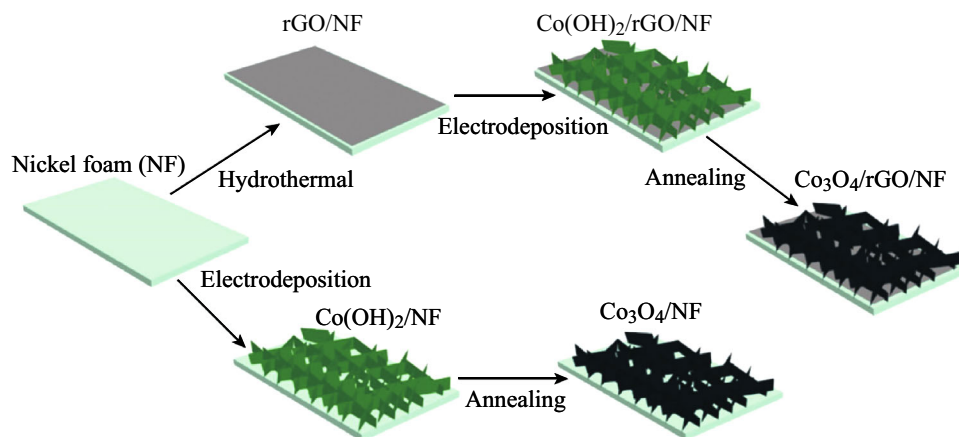


Fig. 1 Schematic of the synthesis procedures of $\text{Co}_3\text{O}_4/\text{rGO}/\text{NF}$ (top) and $\text{Co}_3\text{O}_4/\text{NF}$ (bottom)

Brunauer–Emmett–Teller measurement (BET, ASAP 2020 Micromeritics).

Cyclic voltammetry (CV), galvanostatic charge/discharge (GCD), and electrochemical impedance spectroscopy (EIS) tests are conducted using an electrochemical workstation having a three-electrode configuration. $\text{Co}_3\text{O}_4/\text{rGO}/\text{NF}$ or $\text{Co}_3\text{O}_4/\text{NF}$ is employed as the working electrode using a 1 M KOH electrolyte. The applied potential window of CV measurements ranges from 0.0 to 0.6 V. GCD is performed at a constant current over a fixed potential range of 0.0–0.5 V. The capacitance retention test is performed from 0.0 to 0.5 V at a constant current density of 7 A g^{-1} for 3000 cycles. EIS measurement is performed under an AC voltage with a 5 mV amplitude over a frequency range of 0.01–100 kHz. The specific capacitance C_s (F g^{-1}) is calculated from the GCD data using $C_s = (I\Delta t)/(m\Delta V)$, where I is the charge–discharge current, Δt is the discharge time, m is the mass of Co_3O_4 , and ΔV is the potential change.

3 Results and Discussion

Figure 2a shows the XRD pattern of the $\text{Co}(\text{OH})_2/\text{rGO}/\text{NF}$ structure. The peaks presented in the spectrum match well with those in the standard crystallographic spectrum of layered $\alpha\text{-Co}(\text{OH})_2$ (JCPDS 46-0605) [21], except for the peaks at 44.5° and 51.8° attributed to the NF substrate (JCPDS 87-0712). Figure 2b exhibits the XRD spectra of the products of $\text{Co}(\text{OH})_2/\text{rGO}/\text{NF}$ and $\text{Co}(\text{OH})_2/\text{NF}$ after calcination at 250°C for 2 h, and the XRD pattern of the rGO/NF structure serves as a reference. It is evident that except for the diffraction peaks from NF, all the other peaks are consistent with the (220), (311), (511), and (440) planes in the standard Co_3O_4 pattern (JCPDS 42-1467) [22]. It is worth noting that there are no obvious XRD signals of rGO, possibly because of the low mass loading or destruction of regular stacks of rGO [23].

Figure 2c shows the micro-Raman spectra of rGO/NF, $\text{Co}_3\text{O}_4/\text{NF}$, and $\text{Co}_3\text{O}_4/\text{rGO}/\text{NF}$ composites. Two bands located around 1348.6 and 1609.5 cm^{-1} are assigned to the D and G band of rGO, respectively, indicating that GO has been successfully reduced [24]. For Co_3O_4 -containing samples, five peaks of the crystalline Co_3O_4 phase corresponding to the A_{1g} (691.5 cm^{-1}), F_{2g} (617.7 cm^{-1}), F_{2g} (522.8 cm^{-1}), E_g (482.7 cm^{-1}), and F_{2g} (193.6 cm^{-1}) modes are evident [25], and no obvious characteristic peaks related to $\text{Co}(\text{OH})_2$ can be observed. Accordingly, both XRD and Raman spectra indicate that $\text{Co}(\text{OH})_2$ is completely changed to Co_3O_4 after the aforementioned thermal treatment.

SEM images of rGO/NF, $\text{Co}_3\text{O}_4/\text{NF}$, and $\text{Co}_3\text{O}_4/\text{rGO}/\text{NF}$ are shown in Fig. 3. It is obvious that the rGO coating onto NF is relatively uniform during the hydrothermal reducing process (see Fig. 3a). Figure 3b, c exhibits the top-view SEM images of $\text{Co}_3\text{O}_4/\text{NF}$ and $\text{Co}_3\text{O}_4/\text{rGO}/\text{NF}$, respectively. Interconnected Co_3O_4 nanosheets can be synthesized on both NF and rGO-coated NF. This indicates that the growth of Co_3O_4 nanosheets is dependent more on the growth condition [26] rather than on the substrates. However, compared to the Co_3O_4 nanosheets on NF, the nanosheets on rGO-coated NF have a higher density and lower dimension because of the roughened NF surface due to rGO. Moreover, the corresponding high-magnification SEM images shown in the inset in Fig. 3b, c clearly show that the Co_3O_4 nanosheets on rGO-coated NF are thinner than the ones on NF. Accordingly, compared to $\text{Co}_3\text{O}_4/\text{NF}$, a higher specific surface area can be expected for $\text{Co}_3\text{O}_4/\text{rGO}/\text{NF}$. BET measurement is conducted to examine this hypothesis. Figure 3d shows the N_2 adsorption–desorption isotherms of $\text{Co}_3\text{O}_4/\text{rGO}/\text{NF}$ and $\text{Co}_3\text{O}_4/\text{NF}$. Two distinct hysteresis loops can be observed with a type IV sorption behavior, indicating the presence of a typical mesoporous microstructure for $\text{Co}_3\text{O}_4/\text{rGO}/\text{NF}$ and $\text{Co}_3\text{O}_4/\text{NF}$. The pore size distribution of Co_3O_4 nanosheets on rGO (see the

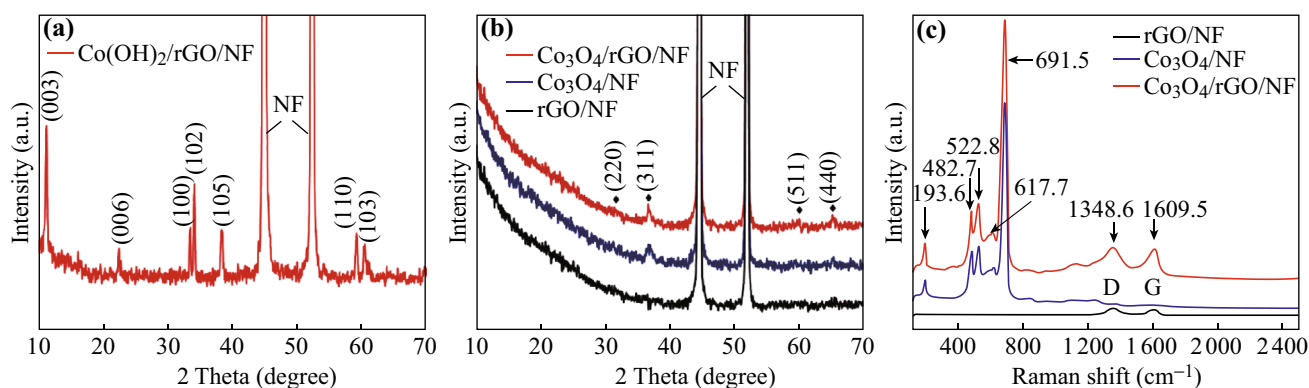


Fig. 2 XRD patterns of **a** Co(OH)₂/rGO/NF and **b** rGO/NF, Co₃O₄/NF, and Co₃O₄/rGO/NF. **c** Micro-Raman spectra of rGO/NF, Co₃O₄/NF, and Co₃O₄/rGO/NF composites

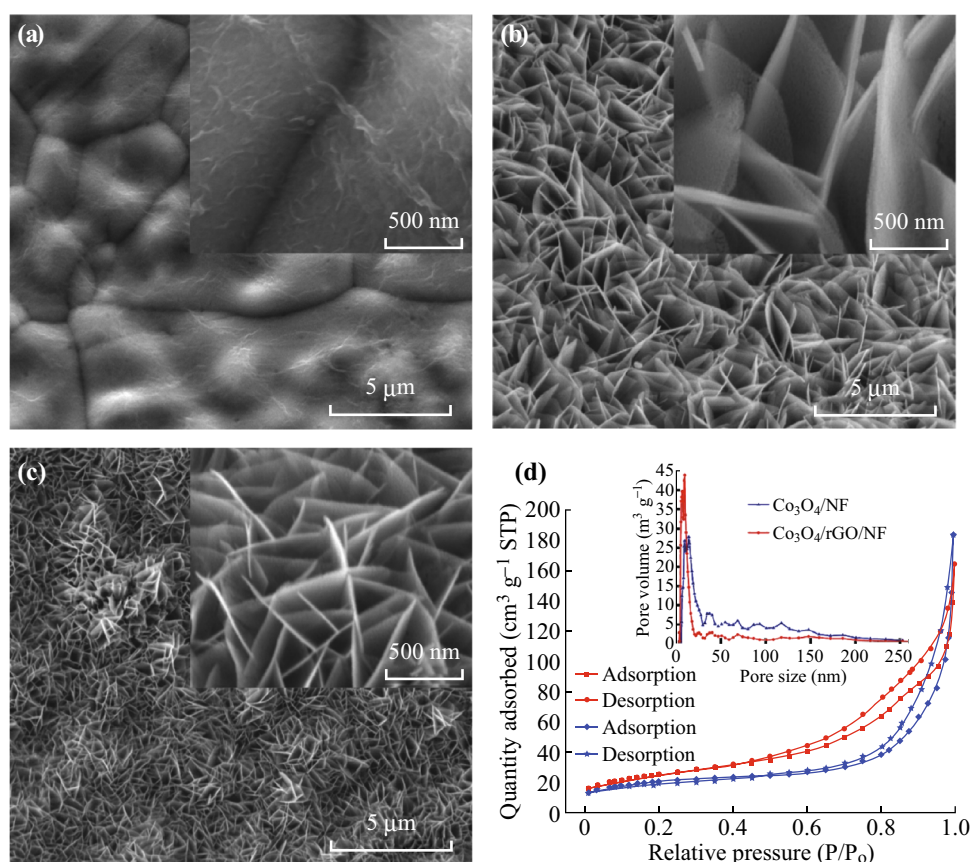


Fig. 3 Top-view SEM images of **a** rGO/NF, **b** Co₃O₄/NF, and **c** Co₃O₄/rGO/NF. **d** N₂ adsorption–desorption isotherms of Co₃O₄/rGO/NF and Co₃O₄/NF. The inset in **d** shows the pore size distribution of both samples

inset of Fig. 3d) indicates that the size of most pores is ~4–15 nm. In contrast, the size of most pores of the Co₃O₄ nanosheets on NF is 6–25 nm. The BET specific areas for Co₃O₄ nanosheets on rGO and on NF are ~87.8 and 67.1 m² g⁻¹, respectively. Accordingly, a higher specific capacitance can be expected for the Co₃O₄/rGO/NF structure.

To reveal further details of the microstructure of the Co₃O₄ nanosheets in Co₃O₄/rGO/NF, HRTEM characterization is performed. As demonstrated in Fig. 4a, the Co₃O₄ nanosheets are composed of small Co₃O₄ nanoparticles of size ~5–15 nm. The lattice fringes as exhibited in Fig. 4b show an interplanar spacing of 0.243 and 0.204 nm, attributed to the (311) and (400) planes of cubic Co₃O₄

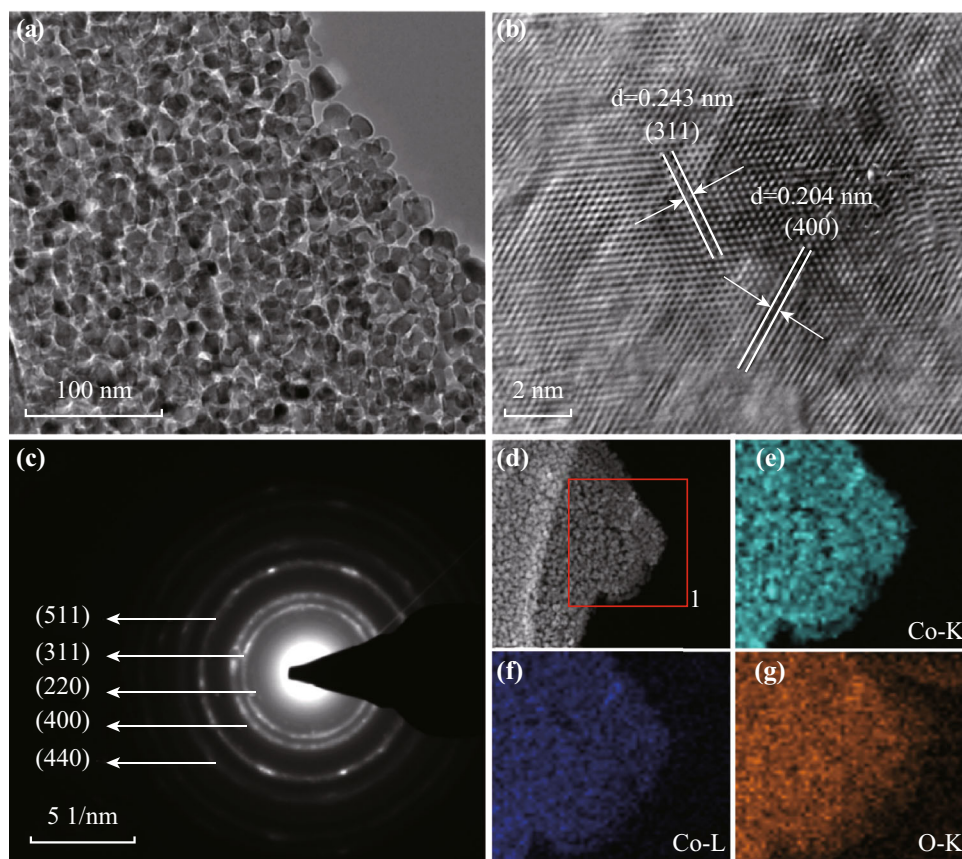


Fig. 4 **a** Low- and **b** high-magnification TEM images, **c** SAED patterns of a Co_3O_4 nanosheet taken from $\text{Co}_3\text{O}_4/\text{rGO}/\text{NF}$. **d** STEM image, and elemental mapping images of **e** and **f** Co and **g** O

[27, 28]. The polycrystalline structure of the obtained Co_3O_4 nanosheets is further confirmed by the selected area electron diffraction (SAED) pattern (see Fig. 4c). The homocentric diffraction rings (from the inside to the outside) can be assigned to the (220), (311), (400), (511), and (440) planes of Co_3O_4 [29]. The elemental distribution in the Co_3O_4 nanosheets is also characterized by scanning transmission electron microscopy (STEM) (see Fig. 4d) and X-ray elemental mapping images (see Fig. 4e–g). The elemental mapping further indicates that Co_3O_4 nanosheets were synthesized successfully.

Figure 5a presents the CV data for NF, rGO/NF, $\text{Co}_3\text{O}_4/\text{NF}$, and $\text{Co}_3\text{O}_4/\text{rGO}/\text{NF}$ under a scanning rate of 3 mV s^{-1} and a potential range of 0.0–0.6 V. It is remarkable that the CV area of $\text{Co}_3\text{O}_4/\text{rGO}/\text{NF}$ is evidently larger than that of $\text{Co}_3\text{O}_4/\text{NF}$ owing to the high specific area of $\text{Co}_3\text{O}_4/\text{rGO}/\text{NF}$ as mentioned above. The redox peaks for the Co_3O_4 -containing samples originate from the conversion of different cobalt oxidation states. Here, it is worth noting that two redox peaks also emerge for NF and rGO/NF, which are attributed to the oxidized surface of NF during heat treatment of $\text{Co}(\text{OH})_2$. However, the contribution of the surface nickel oxide and rGO is not taken into

consideration in the following study because of their negligible capacities compared to the Co_3O_4 -containing samples. This is verified by the calculated areal specific capacitances of 84.0, 120.7, 627.3, and $1107.5 \text{ mF cm}^{-2}$ for NF, rGO/NF, $\text{Co}_3\text{O}_4/\text{NF}$, and $\text{Co}_3\text{O}_4/\text{rGO}/\text{NF}$, respectively, as exhibited in Fig. 5b. The GCD results of $\text{Co}_3\text{O}_4/\text{NF}$ and $\text{Co}_3\text{O}_4/\text{rGO}/\text{NF}$ are exhibited in Fig. 5c, d with current densities of 1, 3, 5, 7, 9, and 10 A g^{-1} and a potential window of 0.0–0.5 V. For each charge/discharge current density, $\text{Co}_3\text{O}_4/\text{rGO}/\text{NF}$ exhibits a larger specific capacitance than $\text{Co}_3\text{O}_4/\text{NF}$. The specific capacitance of $\text{Co}_3\text{O}_4/\text{rGO}/\text{NF}$ is $\sim 1016.4, 872.3, 767.1, 707.2, 657.3,$ and 633.0 F g^{-1} at the corresponding current density of 1–10 A g^{-1} . As a distinct comparison, the $\text{Co}_3\text{O}_4/\text{NF}$ electrode exhibits specific capacitances of 520.0, 513.7, 485.8, 456.8, 444.5, and 435.5 F g^{-1} at the corresponding current densities. Moreover, compared to other previously reported $\text{Co}_3\text{O}_4/\text{rGO}$ composites with different Co_3O_4 microstructures [7, 16, 30], the $\text{Co}_3\text{O}_4/\text{rGO}/\text{NF}$ electrode reported here also delivers superior specific capacitances especially at higher current densities. Here, it is worth noting that the specific capacitance decreases as the charge/discharge current density increases for both $\text{Co}_3\text{O}_4/\text{rGO}/\text{NF}$

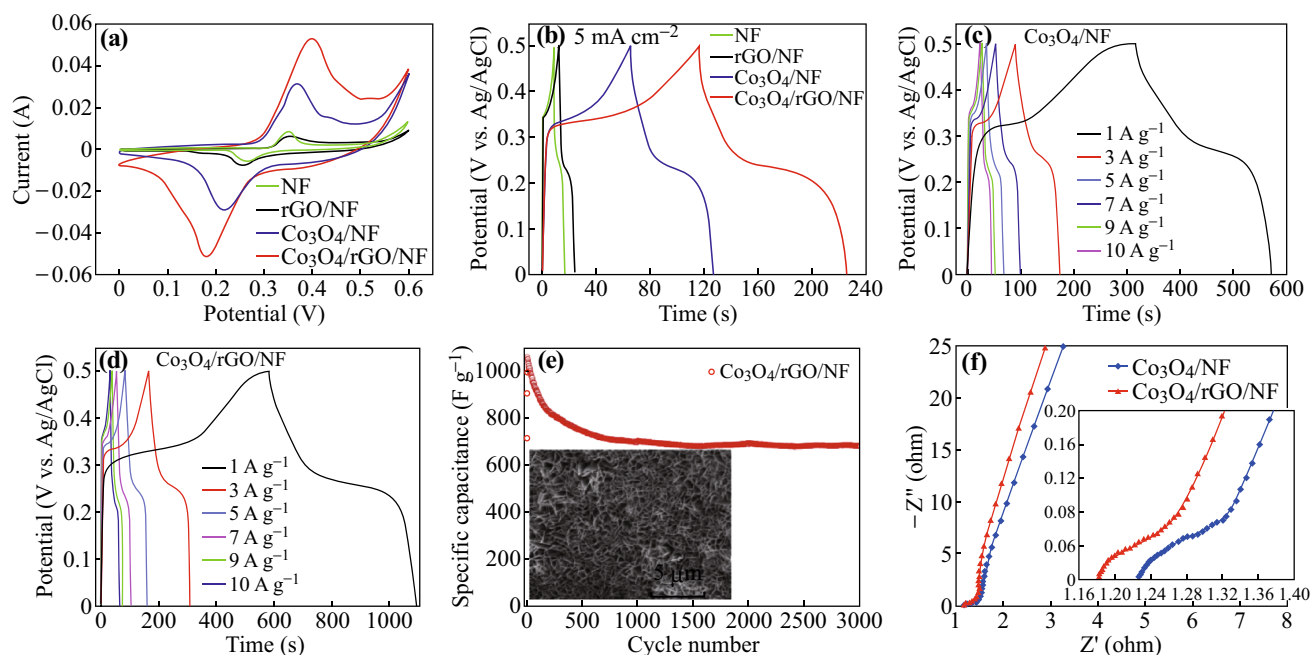


Fig. 5 **a** CV curves of NF, rGO/NF, $\text{Co}_3\text{O}_4/\text{NF}$, and $\text{Co}_3\text{O}_4/\text{rGO}/\text{NF}$ composites at 3 mV s^{-1} . **b** Charge–discharge curves of NF, rGO/NF, $\text{Co}_3\text{O}_4/\text{NF}$, and $\text{Co}_3\text{O}_4/\text{rGO}/\text{NF}$ composites at 5 mA cm^{-2} . Charge–discharge curves of **c** $\text{Co}_3\text{O}_4/\text{NF}$ and **d** $\text{Co}_3\text{O}_4/\text{rGO}/\text{NF}$ at different current densities. **e** Cycling performance of $\text{Co}_3\text{O}_4/\text{rGO}/\text{NF}$ at a current density of 7 A g^{-1} (the inset is a top-view SEM image of $\text{Co}_3\text{O}_4/\text{rGO}/\text{NF}$ after the 3000 cycles shown in **e**). **f** Nyquist plots of $\text{Co}_3\text{O}_4/\text{rGO}/\text{NF}$ and $\text{Co}_3\text{O}_4/\text{NF}$

and $\text{Co}_3\text{O}_4/\text{NF}$. This is because of the insufficient supply of active material [31] and severe polarization [32] at higher current densities. Hence, how to improve the supercapacitive behaviors from these two aspects will be the main consideration in a future study.

To evaluate the cycling performance, the electrochemical stability of $\text{Co}_3\text{O}_4/\text{rGO}/\text{NF}$ and $\text{Co}_3\text{O}_4/\text{rGO}$ is tested using the GCD technique. The cycling performance of $\text{Co}_3\text{O}_4/\text{rGO}/\text{NF}$ at a current density of 7 A g^{-1} is recorded over the potential range of 0.0–0.5 V (see Fig. 5e). For the $\text{Co}_3\text{O}_4/\text{rGO}/\text{NF}$ structure, $\sim 95.5\%$ of the initial specific capacitance can be retained after 3000 cycles even at such a high current density compared to other related reports [7, 33]. However, $\sim 84.4\%$ of the initial specific capacitance is retained after the same cycling period for $\text{Co}_3\text{O}_4/\text{rGO}$. To understand this excellent cycling stability, SEM characterization is performed on the $\text{Co}_3\text{O}_4/\text{rGO}/\text{NF}$ sample after 3000 cycles and is shown in the inset of Fig. 5e. It is obvious that even after 3000 cycles, the microstructure is maintained very well, showing no evident change compared to the microstructures before cycling (see Fig. 3c). It is noted that during the first cycle, there is a significant increase in the specific capacitance. Previous reports mentioned this phenomenon as an activation process [34]. However, such a strong ‘activation’ has been rarely reported and needs to be further investigated to reveal the underlying mechanism.

EIS is used to further understand the electrical properties of the related material/structural system. Figure 5f shows the

Nyquist plots of $\text{Co}_3\text{O}_4/\text{rGO}/\text{NF}$ and $\text{Co}_3\text{O}_4/\text{NF}$. The linear portion of the Nyquist plots in the low-frequency region corresponds to the Warburg impedance, which is related to electrolyte diffusion into the pores in the electrodes. If the impedance plot increases sharply and tends to become a vertical line, it indicates a pure capacitive behavior. In the high-frequency region, the Z' -intercept represents the equivalent series resistance (ESR) including the ionic resistance of the electrolyte, intrinsic resistance of the substrate, and contact resistance at the interface of the active material and current collector [35]. The ESR of $\text{Co}_3\text{O}_4/\text{rGO}/\text{NF}$ and $\text{Co}_3\text{O}_4/\text{NF}$ is ~ 1.18 and 1.22Ω , respectively (see the inset in Fig. 5f), indicating a lower solution resistance and Faradaic resistance for the $\text{Co}_3\text{O}_4/\text{rGO}/\text{NF}$ architecture. In this study, the improved performance of $\text{Co}_3\text{O}_4/\text{rGO}/\text{NF}$ is mainly attributed to the introduction of rGO, which not only provides effective electrolyte accessible channels, thus shortening the ion diffusion distance, but also improves the specific surface area of Co_3O_4 and optimizes the mesopore size distribution for facilitating an enhancement in the capacitance performance.

4 Conclusions

This work reports the effect of rGO on the interconnected Co_3O_4 nanosheets and the improved supercapacitive behaviors. It is found that rGO can help to optimize the

microstructures of the interconnected Co_3O_4 nanosheets, including an increased specific surface area and a more optimal mesopore size distribution, which result in the specific capacitance of the $\text{Co}_3\text{O}_4/\text{rGO}/\text{NF}$ architecture being higher than that of the $\text{Co}_3\text{O}_4/\text{NF}$ structure. Further, the $\text{Co}_3\text{O}_4/\text{rGO}/\text{NF}$ structure possesses excellent cycling stability owing to the improved mechanical and electrical properties associated with the thinned Co_3O_4 nanosheets and incorporation of rGO.

Acknowledgements This work is financially supported from the National Natural Science Foundation of China (Grant Nos.: 61376068, 11304132, 11304133, and 11405144), the Specialized Research Fund of the Doctoral Program of Higher Education (Grant Nos.: 20120211120003 and 20130211120009), and the Fundamental Research Funds for the Central Universities (Grant Nos.: lzujbky-2013-36 and lzujbky-2014-30).

Open Access This article is distributed under the terms of the Creative Commons Attribution 4.0 International License (<http://creativecommons.org/licenses/by/4.0/>), which permits unrestricted use, distribution, and reproduction in any medium, provided you give appropriate credit to the original author(s) and the source, provide a link to the Creative Commons license, and indicate if changes were made.

References

1. P. Simon, Y. Gogotsi, Materials for electrochemical capacitors. *Nat. Mater.* **7**(11), 845–854 (2008). doi:10.1038/nmat2297
2. G. Wang, L. Zhang, J. Zhang, A review of electrode materials for electrochemical supercapacitors. *Chem. Soc. Rev.* **41**(2), 797–828 (2012). doi:10.1039/C1CS15060J
3. D. Li, Y. Gong, M. Wang, C. Pan, Preparation of sandwich-like $\text{NiCo}_2\text{O}_4/\text{rGO}/\text{NiO}$ heterostructure on nickel foam for high performance supercapacitor electrodes. *Nano-Micro Lett.* **9**(2), 16 (2017). doi:10.1007/s40820-016-0117-1
4. M. Kaempgen, C.K. Chan, J. Ma, Y. Cui, G. Gruner, Printable thin film supercapacitors using single-walled carbon nanotubes. *Nano Lett.* **9**(5), 1872–1876 (2009). doi:10.1021/nl8038579
5. J. Deng, L. Kang, G. Bai, Y. Li, P. Li, X. Liu, Y. Yang, F. Gao, W. Liang, Solution combustion synthesis of cobalt oxides (Co_3O_4 and $\text{Co}_3\text{O}_4/\text{CoO}$) nanoparticles as supercapacitor electrode materials. *Electrochim. Acta* **132**, 127–135 (2014). doi:10.1016/j.electacta.2014.03.158
6. T. Geng, L. Zhang, H. Wang, K. Zhang, X. Zhou, Facile synthesis of porous Co_3O_4 nanoplates for supercapacitor applications. *Bull. Mater. Sci.* **38**(5), 1171–1175 (2015). doi:10.1007/s12034-015-0997-6
7. A.N. Naveen, P. Manimaran, S. Selladurai, Cobalt oxide (Co_3O_4)/graphene nanosheets (GNS) composite prepared by novel route for supercapacitor application. *J. Mater. Sci. Mater. Electron.* **26**(11), 8988–9000 (2015). doi:10.1007/s10854-015-3582-2
8. Z. Yang, R. Gao, N. Hu, J. Chai, Y. Cheng, L. Zhang, H. Wei, E.S.-W. Kong, Y. Zhang, The prospective two-dimensional graphene nanosheets: preparation, functionalization, and applications. *Nano-Micro Lett.* **4**(1), 1–9 (2012). doi:10.1007/BF03353684
9. Y. Chen, X. Zhang, D. Yu, Y. Ma, High performance supercapacitors based on reduced graphene oxide in aqueous and ionic liquid electrolytes. *Carbon* **49**(2), 573–580 (2011). doi:10.1016/j.carbon.2010.09.060
10. W.W. Liu, X.B. Yan, J.W. Lang, C. Peng, Q.J. Xue, Flexible and conductive nanocomposite electrode based on graphene sheets and cotton cloth for supercapacitor. *J. Mater. Chem.* **22**(33), 17245–17253 (2012). doi:10.1039/c2jm32659k
11. L. Dong, C. Xu, Q. Yang, J. Fang, Y. Li, F. Kang, High-performance compressible supercapacitors based on functionally synergic multiscale carbon composite textiles. *J. Mater. Chem. A* **3**(8), 4729–4737 (2015). doi:10.1039/C4TA06494A
12. X. Guo, S. Qin, S. Bai, H. Yue, Y. Li, Q. Cheng, J. Li, D. He, Vertical graphene nanosheets synthesized by thermal chemical vapor deposition and the field emission properties. *J. Phys. D-Appl. Phys.* **49**(38), 385301 (2016). doi:10.1088/0022-3727/49/38/385301
13. K. Jost, C.R. Perez, J.K. McDonough, V. Presser, M. Heon, G. Dion, Y. Gogotsi, Carbon coated textiles for flexible energy storage. *Energy Environ. Sci.* **4**(12), 5060–5067 (2011). doi:10.1039/c1ee02421c
14. P. Chen, Y. Su, H. Liu, Y. Wang, Interconnected tin disulfide nanosheets grown on graphene for Li-ion storage and photocatalytic applications. *ACS Appl. Mater. Interfaces* **5**(22), 12073–12082 (2013). doi:10.1021/am403905x
15. C. Xiang, M. Liu, M. Zhi, A. Manivannan, N. Wu, A reduced graphene oxide/ Co_3O_4 composite for supercapacitor electrode. *J. Power Sources* **226**, 65–70 (2013). doi:10.1016/j.jpowsour.2012.10.064
16. C. Yuan, Y. Long, L. Hou, J. Li, Y. Sun, X. Zhang, X. Lu, S. Xiong, X.W.D. Lou, Flexible hybrid paper made of monolayer Co_3O_4 microsphere arrays on rGO/CNTs and their application in electrochemical capacitors. *Adv. Funct. Mater.* **22**(12), 2560–2566 (2012). doi:10.1002/adfm.201102860
17. T.T. Nguyen, V.H. Nguyen, R.K. Deivasigamani, D. Kharismadewi, Y. Iwai, J.-J. Shim, Facile synthesis of cobalt oxide/reduced graphene oxide composites for electrochemical capacitor and sensor applications. *Solid State Sci.* **53**, 71–77 (2016). doi:10.1016/j.solidstatesciences.2016.01.006
18. D.C. Marcano, D.V. Kosynkin, J.M. Berlin, A. Sinitskii, Z. Sun, A. Slesarev, L.B. Alemany, W. Lu, J.M. Tour, Improved synthesis of graphene oxide. *ACS Nano* **4**(8), 4806–4814 (2010). doi:10.1021/nn1006368
19. Y. Sun, W. Zhang, D. Li, L. Gao, C. Hou, Y. Zhang, Y. Liu, Facile synthesis of $\text{MnO}_2/\text{rGO}/\text{Ni}$ composite foam with excellent pseudocapacitive behavior for supercapacitors. *J. Alloys Compd.* **649**, 579–584 (2015). doi:10.1016/j.jallcom.2015.07.212
20. Y. Zou, I.A. Kinloch, R.A.W. Dryfe, Mesoporous vertical Co_3O_4 nanosheet arrays on nitrogen-doped graphene foam with enhanced charge-storage performance. *ACS Appl. Mater. Interfaces* **7**(41), 22831–22838 (2015). doi:10.1021/acsami.5b05095
21. J.-H. Zhong, A.-L. Wang, G.-R. Li, J.-W. Wang, Y.-N. Ou, Y.-X. Tong, $\text{Co}_3\text{O}_4/\text{Ni}(\text{OH})_2$ composite mesoporous nanosheet networks as a promising electrode for supercapacitor applications. *J. Mater. Chem.* **22**(12), 5656–5665 (2012). doi:10.1039/c2jm15863a
22. X.-C. Dong, H. Xu, X.-W. Wang, Y.-X. Huang, M.B. Chan-Park, H. Zhang, L.-H. Wang, W. Huang, P. Chen, 3D Graphene–cobalt oxide electrode for high-performance supercapacitor and enzymeless glucose detection. *ACS Nano* **6**, 3206–3213 (2012). doi:10.1021/mn300097q
23. L. Wang, X. Wang, X. Xiao, F. Xu, Y. Sun, Z. Li, Reduced graphene oxide/nickel cobaltite nanoflake composites for high specific capacitance supercapacitors. *Electrochim. Acta* **111**, 937–945 (2013). doi:10.1016/j.electacta.2013.08.094
24. L. Athouël, F. Moser, R. Dugas, O. Crosnier, D. Bélanger, T. Brousse, Variation of the MnO_2 birnessite structure upon charge/discharge in an electrochemical supercapacitor electrode in aqueous Na_2SO_4 electrolyte. *J. Phys. Chem. C* **112**(18), 7270–7277 (2008). doi:10.1021/jp0773029

25. B. Varghese, C.H. Teo, Y. Zhu, M.V. Reddy, B.V.R. Chowdari, A.T.S. Wee, V.B.C. Tan, C.T. Lim, C.H. Sow, Co_3O_4 nanostructures with different morphologies and their field-emission properties. *Adv. Funct. Mater.* **17**(12), 1932–1939 (2007). doi:[10.1002/adfm.200700038](https://doi.org/10.1002/adfm.200700038)
26. A.D. Jagadale, V.S. Kumbhar, R.N. Bulakhe, C.D. Lokhande, Influence of electrodeposition modes on the supercapacitive performance of Co_3O_4 electrodes. *Energy* **64**, 234–241 (2014). doi:[10.1016/j.energy.2013.10.016](https://doi.org/10.1016/j.energy.2013.10.016)
27. C. Yuan, L. Yang, L. Hou, L. Shen, X. Zhang, X.W. Lou, Growth of ultrathin mesoporous Co_3O_4 nanosheet arrays on Ni foam for high-performance electrochemical capacitors. *Energy Environ. Sci.* **5**(7), 7883–7887 (2012). doi:[10.1039/c2ee21745g](https://doi.org/10.1039/c2ee21745g)
28. W. Hong, J. Wang, Z. Li, S. Yang, Fabrication of Co_3O_4 @Co-Ni sulfides core/shell nanowire arrays as binder-free electrode for electrochemical energy storage. *Energy* **93**, 435–441 (2015). doi:[10.1016/j.energy.2015.09.053](https://doi.org/10.1016/j.energy.2015.09.053)
29. S. Min, C. Zhao, G. Chen, Z. Zhang, X. Qian, One-pot hydrothermal synthesis of 3D flower like $\text{rGO}/\text{Co}_3\text{O}_4/\text{Ni}(\text{OH})_2$ composite film on nickel foam for high-performance supercapacitors. *Electrochim. Acta* **135**, 336–344 (2014). doi:[10.1016/j.electacta.2014.05.032](https://doi.org/10.1016/j.electacta.2014.05.032)
30. C.Z. Yuan, L. Zhang, L. Hou, G. Pang, W.-C. Oh, One-step hydrothermal fabrication of strongly coupled Co_3O_4 nanosheets–reduced graphene oxide for electrochemical capacitors. *RSC Adv.* **4**(28), 14408–14413 (2014). doi:[10.1039/c4ra00762j](https://doi.org/10.1039/c4ra00762j)
31. Y.G. Zhu, Y. Wang, Y. Shi, Z.X. Huang, L. Fu, H.Y. Yang, Phase transformation induced capacitance activation for 3D graphene-CoO nanorod pseudocapacitor. *Adv. Energy Mater.* **4**(9), 1079–1098 (2014). doi:[10.1002/aenm.201301788](https://doi.org/10.1002/aenm.201301788)
32. B. Wang, X. He, H. Li, Q. Liu, J. Wang, L. Yu, H. Yan, Z. Li, P. Wang, Optimizing the charge transfer process by designing Co_3O_4 @PPy@ MnO_2 ternary core-shell composite. *J. Mater. Chem. A* **2**(32), 12968–12973 (2014). doi:[10.1039/C4TA02380C](https://doi.org/10.1039/C4TA02380C)
33. M. Jing, Y. Yang, Y. Zhu, H. Hou, Z. Wu, X. Ji, An asymmetric ultracapacitors utilizing α - $\text{Co}(\text{OH})_2/\text{Co}_3\text{O}_4$ flakes assisted by electrochemically alternating voltage. *Electrochim. Acta* **141**, 234–240 (2014). doi:[10.1016/j.electacta.2014.07.075](https://doi.org/10.1016/j.electacta.2014.07.075)
34. X. Xia, J. Tu, Y. Zhang, X. Wang, C. Gu, X.-B. Zhao, H.J. Fan, High-quality metal oxide core/shell nanowire arrays on conductive substrates for electrochemical energy storage. *ACS Nano* **6**(6), 5531–5538 (2012). doi:[10.1021/nn301454q](https://doi.org/10.1021/nn301454q)
35. X. Chen, F. Zhang, Z. Yang, S. Huang, One-pot hydrothermal synthesis of reduced graphene oxide/carbon nanotube/ α - $\text{Ni}(\text{OH})_2$ composites for high performance electrochemical supercapacitor. *J. Power Sources* **243**, 555–561 (2013). doi:[10.1016/j.jpowsour.2013.04.076](https://doi.org/10.1016/j.jpowsour.2013.04.076)